

A metallography and x-ray tomography study of spall damage in ultrapure Al

M. L. Qi, B. X. Bie, F. P. Zhao, C. M. Hu, D. Fan, X. X. Ran, X. H. Xiao, W. G. Yang, P. Li, and S. N. Luo

Citation: *AIP Advances* **4**, 077118 (2014); doi: 10.1063/1.4890310

View online: <http://dx.doi.org/10.1063/1.4890310>

View Table of Contents: <http://scitation.aip.org/content/aip/journal/adva/4/7?ver=pdfcov>

Published by the *AIP Publishing*

Articles you may be interested in

[Nucleation and growth of damage in polycrystalline aluminum under dynamic tensile loading](#)

AIP Advances **5**, 037116 (2015); 10.1063/1.4914919

[X-ray computerized tomography scan of crumpled aluminum sheet](#)

Chaos **19**, 041109 (2009); 10.1063/1.3212924

[Stress-induced phenomena in nanosized copper interconnect structures studied by x-ray and electron microscopy](#)

J. Appl. Phys. **106**, 093711 (2009); 10.1063/1.3254166

[Electromigration in passivated Cu interconnects studied by transmission x-ray microscopy](#)

J. Vac. Sci. Technol. B **20**, 3089 (2002); 10.1116/1.1523403

[Interfacial reaction pathways and kinetics during annealing of 111-textured Al/TiN bilayers: A synchrotron x-ray diffraction and transmission electron microscopy study](#)

J. Vac. Sci. Technol. A **19**, 2207 (2001); 10.1116/1.1379800

An advertisement for AIP's journal of computational tools and methods. It features a row of tablet devices displaying the journal's cover, which shows a colorful, abstract image. The text 'computing' is written in a stylized font, with 'SCIENCE & ENGINEERING' underneath. Below the tablets, the text 'AIP'S JOURNAL OF COMPUTATIONAL TOOLS AND METHODS. AVAILABLE AT MOST LIBRARIES.' is displayed in a large, white, sans-serif font. The background is a blurred image of a library or study area.

A metallography and x-ray tomography study of spall damage in ultrapure Al

 HPSTAR
 081_2014

 M. L. Qi,^{1,2} B. X. Bie,^{1,3} F. P. Zhao,³ C. M. Hu,^{2,4} D. Fan,³ X. X. Ran,¹
 X. H. Xiao,⁵ W. G. Yang,^{2,a} P. Li,⁴ and S. N. Luo^{3,b}
¹*School of Science, Wuhan University of Technology, Wuhan, Hubei 430070, P. R. China*
²*HPSynC@Advanced Photon Source, Argonne National Laboratory, Argonne, Illinois 60439, USA*
³*The Peac Institute of Multiscale Sciences and Sichuan University, Chengdu, Sichuan 610207, P. R. China*
⁴*National Key Laboratory of Shock Wave and Detonation Physics, Chinese Academy of Engineering Physics, Mianyang, Sichuan 621900, P. R. China*
⁵*Advanced Photon Source, Argonne National Laboratory, Argonne, Illinois 60439, USA*

(Received 6 June 2014; accepted 2 July 2014; published online 14 July 2014)

We characterize spall damage in shock-recovered ultrapure Al with metallography and x-ray tomography. The measured damage profiles in ultrapure Al induced by planar impact at different shock strengths, can be described with a Gaussian function, and showed dependence on shock strengths. Optical metallography is reasonably accurate for damage profile measurements, and agrees within 10–25% with x-ray tomography. Full tomography analysis showed that void size distributions followed a power law with an exponent of $\gamma = 1.5 \pm 2.0$, which is likely due to void nucleation and growth, and the exponent is considerably smaller than the predictions from percolation models. © 2014 Author(s). All article content, except where otherwise noted, is licensed under a Creative Commons Attribution 3.0 Unported License. [<http://dx.doi.org/10.1063/1.4890310>]

I. INTRODUCTION

Damage of ductile metals under high strain rate loading has long been studied with planar shock loading. Void nucleation and growth coupled with plasticity, are responsible for shock-induced spallation damage, and such information is extremely useful for developing physics-based, dynamic damage models.^{1–5} However, in situ, real time measurements are largely limited to free surface or target-window interface velocities, since the technical challenges still render such measurements a formidable task on void evolution in ductile metals. Thus, damage characterization has heavily relied on shock-recovered samples, which are normally examined with optical metallography, scanning and transmission electron microscopy, and electron backscattered diffraction.^{6–10} These techniques are mostly two-dimensional (2D) in nature, and one has to resort to serial sectioning, or stereographic techniques such as the Schwartz-Saltykov method, to obtain 3D information.^{11–15}

Recently, synchrotron x-ray tomography has been utilized to characterize materials including shock-recovered samples.^{9,16–18} This non-destructive technique can resolve individual voids at micron scale and thus true damage characteristics in shock-spalled samples, but it is under exploited. Void size distributions and spall damage profiles along the shock direction are important constraints on developing damage models for high-strain rate loading. Given the simplicity and convenience of 2D metallography methods, it is also of interest to quantify the errors in damage profile measurements against true values. Here we use 2D optical metallography and 3D x-ray tomography to examine damage in shock-recovered, ultrapure Al samples, to obtain 1D damage profiles and

^awenge@aps.anl.gov

^bsluo@pims.ac.cn.


TABLE I. Shot parameters. u_{flyer} : impact or flyer velocity; P_{H} : peak shock stress; D_{max} : the maximum damage, σ : variance, and x_0 : expected value in a Gaussian fit[Eq. (7)]; FWHM: full-width at half maximum; 2D: 2D metallography; 3D: 3D x-ray tomography; γ : power-law exponent.

Sample No.	u_{flyer} (ms^{-1})	P_{H} (GPa)	$D_{\text{max,2D}}$	$D_{\text{max,3D}}$	$\sigma_{2\text{D}}$ (mm)	$\sigma_{3\text{D}}$ (mm)	$x_{0,2\text{D}}$ (mm)	$x_{0,3\text{D}}$ (mm)	FWHM _{2D} (mm)	FWHM _{3D} (mm)	γ
Al010b	149.6	1.01	0.032	0.007	0.36	0.38	3.11	3.04	0.85	0.89	1.18 ± 0.14
Al022b	170.0	1.31	0.155	0.274	0.41	0.15	3.05	3.03	0.97	0.35	1.44 ± 0.06
Al006b	196.9	1.53	0.209	0.273	0.27	0.25	2.91	3.07	0.64	0.59	1.57 ± 0.18
Al007b	201.0	1.55	0.250	0.332	0.21	0.18	2.94	3.03	0.49	0.42	1.65 ± 0.08
Al005b	215.4	1.67	0.278	0.291	0.36	0.29	2.89	3.01	0.85	0.68	1.24 ± 0.13
Al003b	236.3	1.80	0.436	0.367	0.37	0.32	3.01	2.96	0.87	0.75	1.61 ± 0.14

3D void distributions, and gain insights into void nucleation and growth processes. The damage profiles for different shock strengths are characterized with both methods, and the 2D metallography is reasonably accurate for describing damage zone width and the maximum damage. Our knowledge on void size distribution is extremely limited, and the only experimental report is on laser-shocked Ta single crystals.¹⁸ Our measurements show power-law void size distributions with an exponent of $\gamma = 1.5 \pm 2.0$. Section II addresses experiments and data analyses, followed by results and discussion in Sec. III, and summary and conclusion in Sec. IV.

II. EXPERIMENTS AND DATA PROCESSING

A. Plate impact shock wave experiments

Plate-impact experiments were performed on a light gas gun with a 100-mm bore diameter. The flyer plate (u_{flyer}) velocity was measured with magnetic coils, and the target free surface velocity, with a velocity interferometer through a small hole about 5 mm in diameter at the back of the recovery chamber. The accuracy in velocity was better than 1%. Both samples and flyer plates were made from an ultrapure Al rod (99.999% purity). The thickness ratio of the flyer plates and targets can be varied to control the spall plane location (x_0) in the target. The diameters of the flyer plates and targets were 48 mm, except for shot Al022b (38 mm). Their thicknesses were 3 mm and 6 mm, respectively. These dimensions were chosen to minimize the edge effect resulting from radial release, which was negligible in the central region of the soft-recovered samples. Impact-induced shock waves propagated in both directions, which were then reflected as release fans from the flyer-sabot interface or target free surface. The interactions of the release fans led to tension and spallation in the targets. The targets (samples) were soft-recovered for optical metallography and x-ray tomography. The experimental parameters are listed in Table I. More details on shock loading and recovery can be found in Ref. 19.

B. Damage evaluation with 2D optical metallography

The soft-recovered samples were cut into two even halves along the shock direction with electrical-discharge machining. The cut surface of one half was ground using fine sandpapers, and then polished to mirror finish with diamond slurry ($1\mu\text{m}$) on a semi-automatic polishing machine. The polished crosssections were examined with an optical metallurgical microscope. Figs. 1 and 2 show some typical micrographs, where the voids are displayed as black dots.

Damage characteristics from 2D metallography were obtained as follows. A micrograph was divided evenly into multiple zones along sample thickness direction [Fig. 3(a)]. The zone width was sufficiently small for a good spatial resolution, but wide enough to contain a reasonable amount of voids for a statistical analysis of voids. The number of zones was between 20 and 30. The void size-number distribution (histogram) in each zone were obtained from image processing. For each

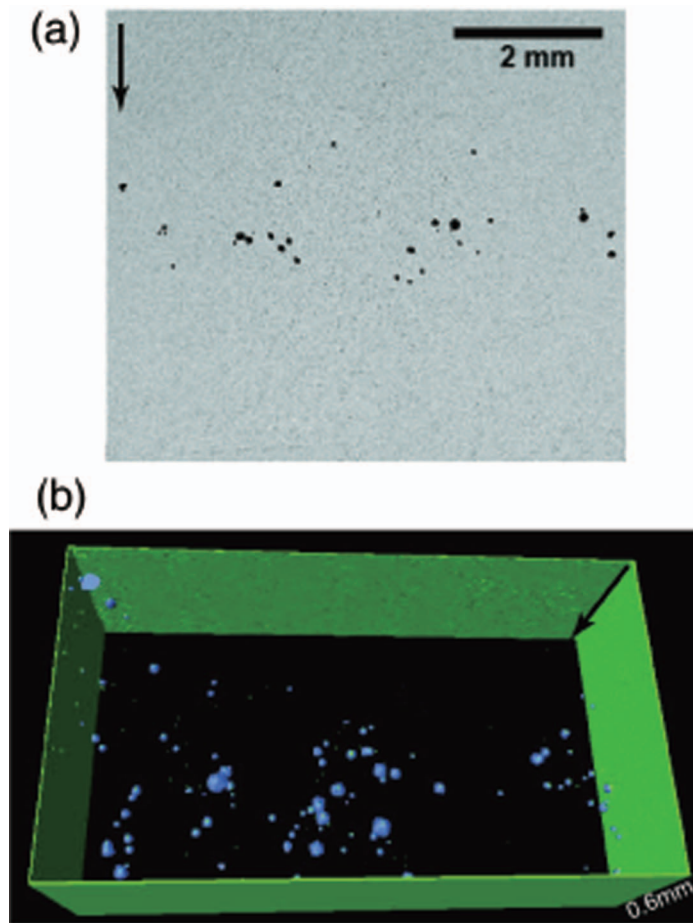


FIG. 1. 2D and 3D void distributions in shock-recovered pure Al sample Al010b ($u_{\text{flyer}} = 149.6$ m/s): (a) An optical micrograph of a cross-section. (b) A 0.6 mm thick slice from x-ray tomography, cut perpendicular to the shock direction. The arrows indicate shock direction. The box dimensions in (b) are 0.6 mm \times 2 mm \times 2 mm.

zone, we applied the widely used Schwartz-Saltykov method of stereoscopic metallography for estimating the volume fraction of 3D voids from a measured histogram of 2D voids.^{11,12,14,15}

We follow Hilliard and Lawson's nomenclature and derivation¹⁵ to discuss briefly the Schwartz-Saltykov method, assuming spherical particles (voids here). The particle sizes and intercept sizes are divided into an equal number (k) of bins. The largest intercept size is $2R_{\text{max}}$; the bin size $\Delta = 2R_{\text{max}}/k$, a basic size units for both particles and intercepts. We use subscripts i and j to index discrete diameter sizes for intercepts and particles, respectively. Each bin contains intercepts in the interval $[(i-1)\Delta, i\Delta]$, or particle sizes in $[(j-1)\Delta, j\Delta]$. The number of intercepts per unit area (A) in the i th bin is $NA(i)$, and the volumetric (V) counterpart is $NV(j)$.

The number of intercepts with size i per unit area due to size j particles is

$$N_A(i, j) = P(i, j)N_A(j) = N_V(j)(2R_j)F_i \quad (1)$$

Here $P(i, j)$ is the probability that an intercept of classification i results, given that the cutting plane intercepts a particle of size j ; $NA(j)$ refers to the intercepts with particles of size j ; $2R_j$ is the mean caliper diameter of bodies of size j , and F_i is the integrated density function for intercepts. The above equation is further reduced to

$$N_A(i, j) = N_V(j)\Delta\alpha_{ij} \quad (2)$$

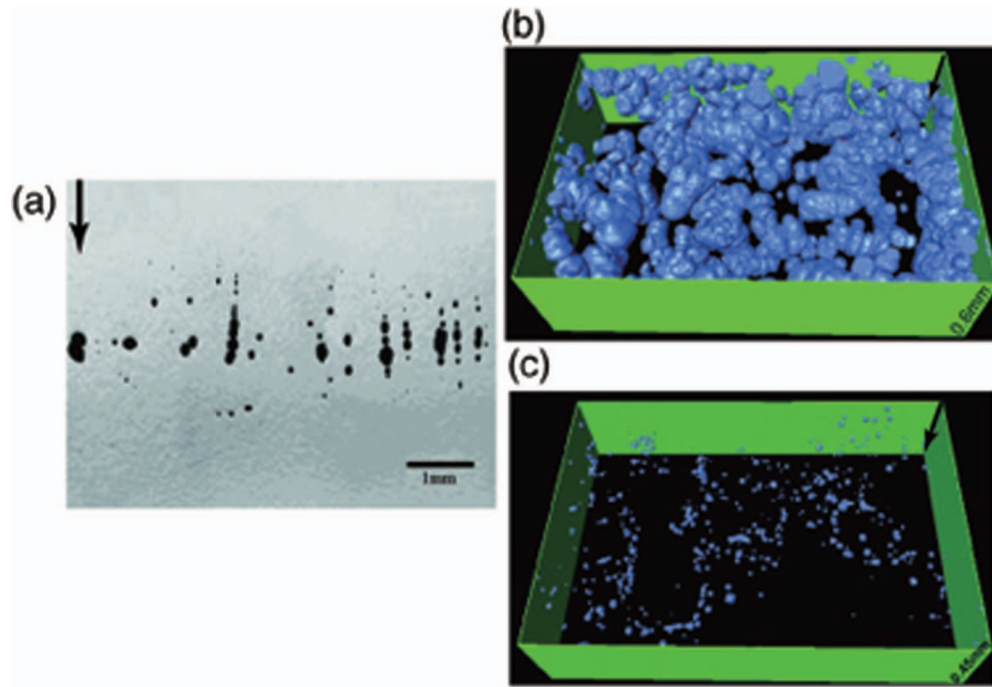


FIG. 2. 2D and 3D void distributions in shock-recovered pure Al sample Al006b ($u_{\text{flyer}} = 196.9$ m/s): (a) An optical micrograph of a cross-section. (b) A 0.6 mm thick slice near the spall plane and (c) a 0.45 mm thick slice far from the spall plane, cut perpendicular to the shock direction. The box dimensions in (b) and (c) are $0.6 \text{ mm} \times 2 \text{ mm} \times 2 \text{ mm}$ and $0.45 \text{ mm} \times 2 \text{ mm} \times 2 \text{ mm}$, respectively. The arrows indicate shock direction.

with

$$\alpha_{ij} = \sqrt{j^2 - (i-1)^2} - \sqrt{j^2 - i^2}, \quad j \geq i \quad (3)$$

Then,

$$N_A(i) = \sum_{j \geq i} N_A(i, j) = \Delta \sum_{j \geq i} N_V(j) \alpha_{i, j} \quad (4)$$

which can be rewritten in matrix and vector forms as

$$N_V = \frac{1}{\Delta} [\alpha_{ij}]^{-1} N_A \quad (5)$$

where $[\alpha_{ij}]$ is a lower triangular matrix. This equation states that 3D size distributions of particles can be obtained from 2D distributions of intercepts on a cutting plane.

For shock recovered samples, the collective damage within a zone is defined as the volume fraction of particles or voids

$$D = \sum_j \frac{4}{3} \pi R_j^3 N_V(j) \quad (6)$$

The 1D damage or porosity profiles, $D(x)$, along the sample thickness or shock direction were then obtained. Here x is the distance from sample free surface.

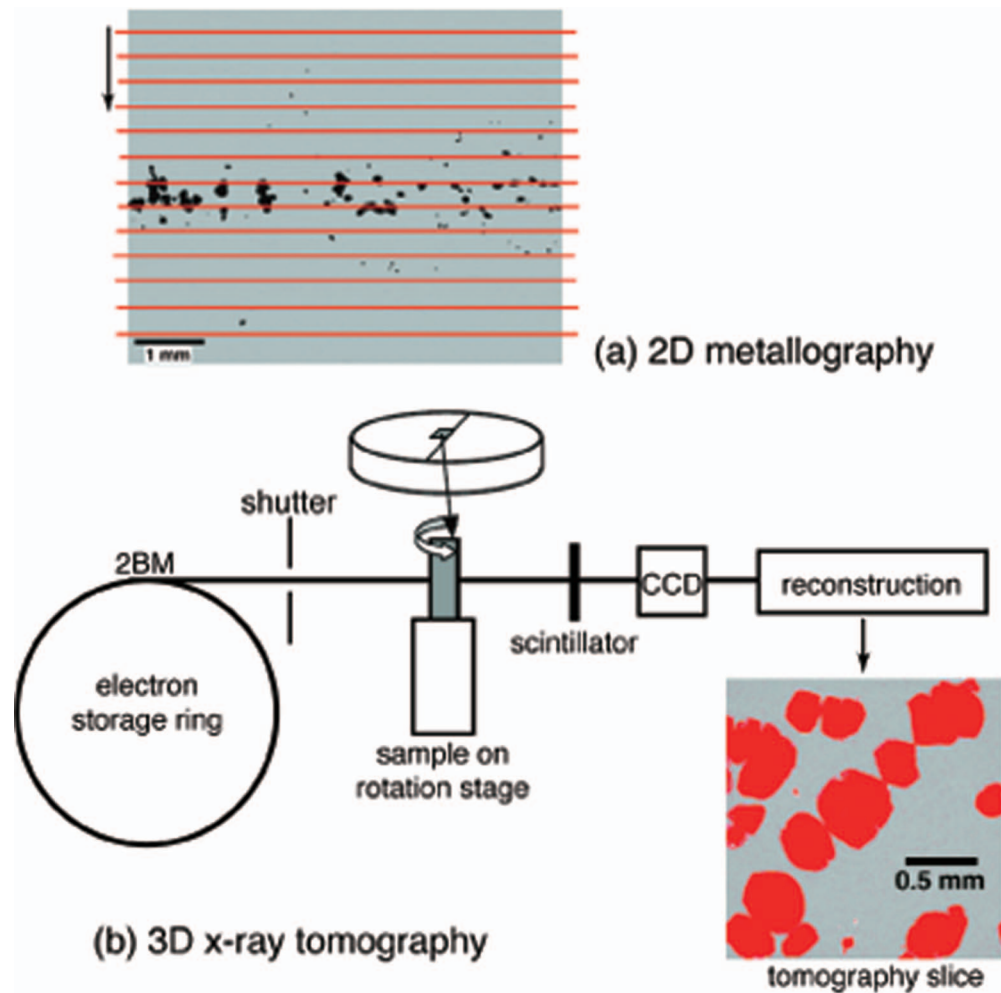


FIG. 3. (a) Illustration of 2D metallography for measuring damage profiles (the micrograph is for Al022b). (b) Schematic for 3D x-ray tomography at the APS (Advanced Photon Source) beamline 2BM. CCD: charge coupled device. The arrow in (a) indicates shock direction.

C. 3D x-ray tomography

High resolution x-ray tomography was conducted on the “soft-recovered” samples using the tomography system at the beamline 2BM of the Advanced Photon Source (APS), Argonne National Laboratory [Fig. 1(b)]. The beam spot size at 2BM upstream was about $3.5 \text{ mm} \times 15 \text{ mm}$. The energy range of the x-ray beam at 2BM was selectable between 5 and 20 keV by the use of a Kohzu double-crystal monochromator. To characterize the spatial distribution of damage along the thickness direction, a rectangular cuboid ($6 \text{ mm} \times 2 \text{ mm} \times 2 \text{ mm}$) was cut from the middle section of one half of the shocked sample. Because the cuboid was rotated during tomography, the thickness traversed by x-rays was between 2 mm to 2.828 mm, corresponding to a transmission of 18% and 10% at 20keV, respectively; the thickness along the x-ray direction should be below 3 mm for a reasonable signal-to-noise ratio.

The sample was mounted on a standard kinematic mount and rotation was achieved with a high-precision rotation stage. The x-rays were transmitted through the sample and detected with a CdWO₄ scintillator, which converted the x-rays to visible light. The light was collected by a 2048×2048 pixel CoolSnap K4 CCD camera through a microscope objective lens. The system was capable of capturing high resolution images (spatial resolution $\sim 1 \mu\text{m}$) while concurrently obtaining 180 of projection data. The exposure time was between 80 and 200 ms per projection. A

total of 1504 projections with an angular step size of $\frac{1}{8}^\circ$ for each sample were collected. Once the tomographic data was collected, a group of slices were created using inverse Fourier transformation, and imported to ImageJ²⁰ to adjust image contrast. These images were composed and rendered into a 3D representation of the sample by the software AmiraTM (Indeen-Visual Concepts GmbH). Some examples of reconstructed and rendered images are shown in Figs. 2(b), 3(b), and 3(c).

Each sample with a thickness of 6 mm included 4,000 slices in the thickness direction. All slices were divided into 200 groups with an equal distance ($30\mu\text{m}$) in the thickness direction (x). Therefore, each group included 20 slices. The slices in each group were used to calculate porosity and 200 damage values (D) were calculated for each sample to obtain porosity, i.e., the relative void volume, or damage D within a $30\mu\text{m}$ thickness along the sample thickness direction, and thus the damage profiles, $D(x)$.

III. RESULTS AND DISCUSSION

Six plate impact shock-recovery experiments were conducted at different flyer velocities ($u_{\text{flyer}} = 149.6\text{m/s}-236.3\text{m/s}$), intended to cover incipient to intermediate spall damage. The soft-recovered samples were examined with 2D metallography and 3D x-ray tomography, and results are shown in Figs. 2–6 and Table I.

Continuum-level simulations are useful for developing damage models and predicting shock responses. An important constraint from experiments is the damage profiles along the sample thickness direction, i.e., $D(x)$ at different shock strengths. Figure 4 shows such profiles obtained both from 2D optical metallography and 3D x-ray tomography (referred to as 2D and 3D, respectively, for simplicity). At the lowest u_{flyer} (149.6 m/s, Al1010b), the 2D profile is asymmetric while the 3D profile is highly symmetric [Figs. 4(a) and 4(b)]. Both profiles display multiple small peaks, which could be due to isolated voids or multiple spallations. At higher shock strengths, the general features for both 2D and 3D profiles are all similar: the profiles are smooth with a Gaussian shape. For example, the voids in Fig. 2 (149.6 m/s) are smaller and more isolated compared to those in Fig. 3 (196.9 m/s), and thus $D(x)$ is less smooth in the former case. With increasing shock strength, the void size increases from μm level to 100's μm , so do void quantity and D , for instance, at the spall plane. For a given shot, both damage and void size decrease as the location under consideration moves away from the spall plane (nominally at $x = 3$ mm) as seen, e.g., from Fig. 3(a) for $u_{\text{flyer}} = 196.9$ m/s.

To quantify the damage profiles $D(x)$, we fit the measurements with a Gaussian function,

$$D(x) = D_{\text{max}} \exp \left\{ -\frac{(x - x_0)^2}{2\sigma^2} \right\}, \quad (7)$$

where D_{max} denotes the maximum damage, and x_0 is the mean and σ is the variance of the damage distribution. Physically, x_0 and σ indicate spall plane location and characteristic damage zone width, respectively. We also calculate the full-width at half maximum of the damage zone as $\text{FWHM} = 2\sigma\sqrt{2\ln 2}$. The fitting results are shown in Fig. 4, and the parameters listed in Table I. It seems that spall damage profiles can be well described with a Gaussian. Such profiles were also observed in molecular dynamics simulations of single crystal Cu.²¹

Figure 5 shows the damage profile parameters for different shock strengths or peak stresses. The 3D results [Figs. 5(b), 5(d), and 5(f)] suggest that to the first order approximation, the maximum damage and damage zone width increase, while the spall plane location decreases, with increasing strength. The broad damage width at the incipient spall may be due to the tensile stress profile ($u_{\text{flyer}} = 149.6$ m/s), and the decrease in x_0 can be caused by compression. The 2D results are consistent, except that the damage zone width does not show a clear trend, and one reason could be the large measurement scatter inherent in this 2D method.

An important advantage of 2D metallography lies in its simplicity in measurements and data processing. This 2D optical method deduces 3D size distributions from surface measurements via, for example, the Schwartz–Saltykov method, does not require such large x-ray facilities as synchrotrons, and is widely used in materials characterization including spall damage.¹ The 3D x-ray tomography

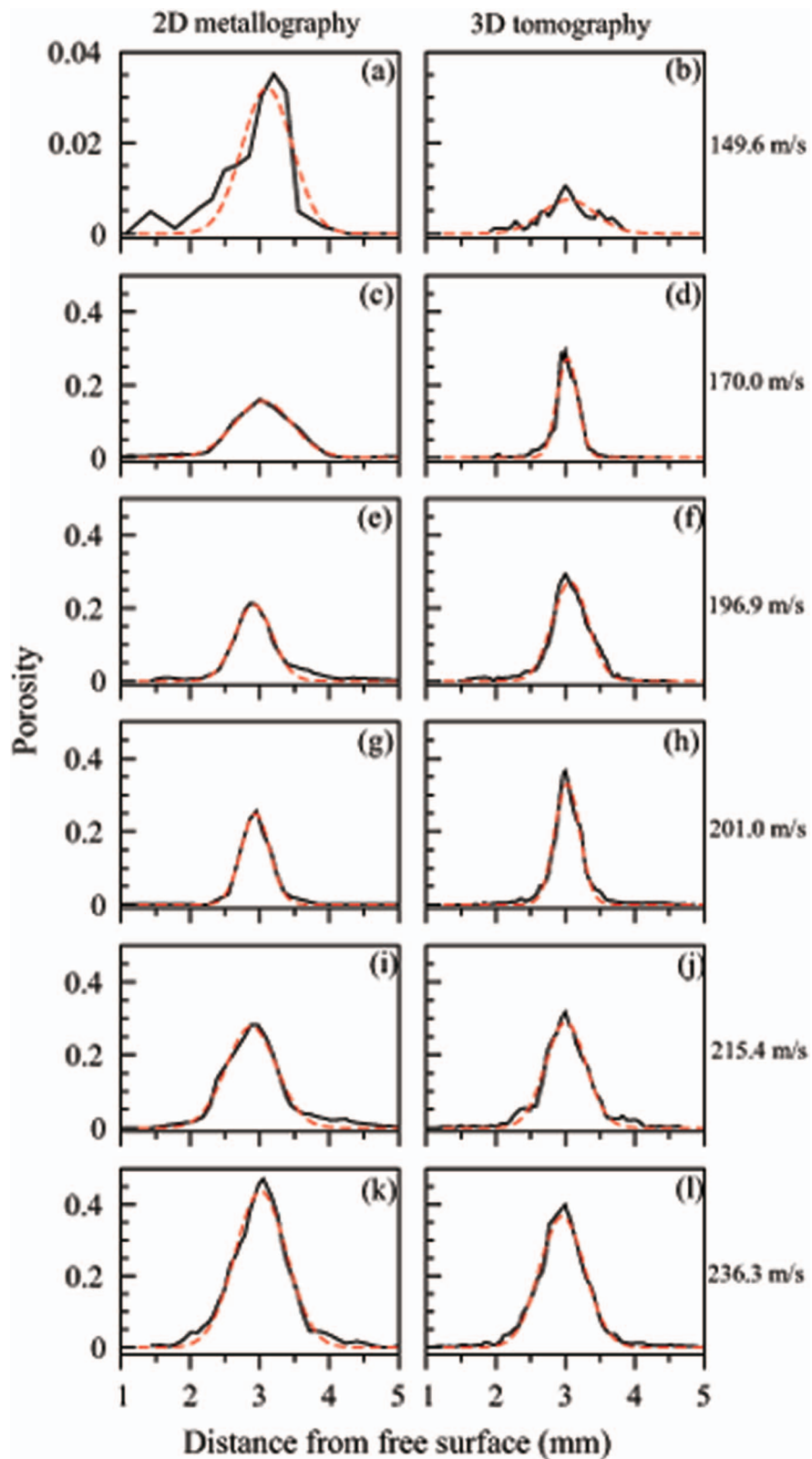


FIG. 4. Porosity or damage profiles, $D(x)$, measured with 2D metallography (left column) and 3D x-ray tomography (right column), and their Gaussian fits (dashed curves) at different impact velocities as indicated.

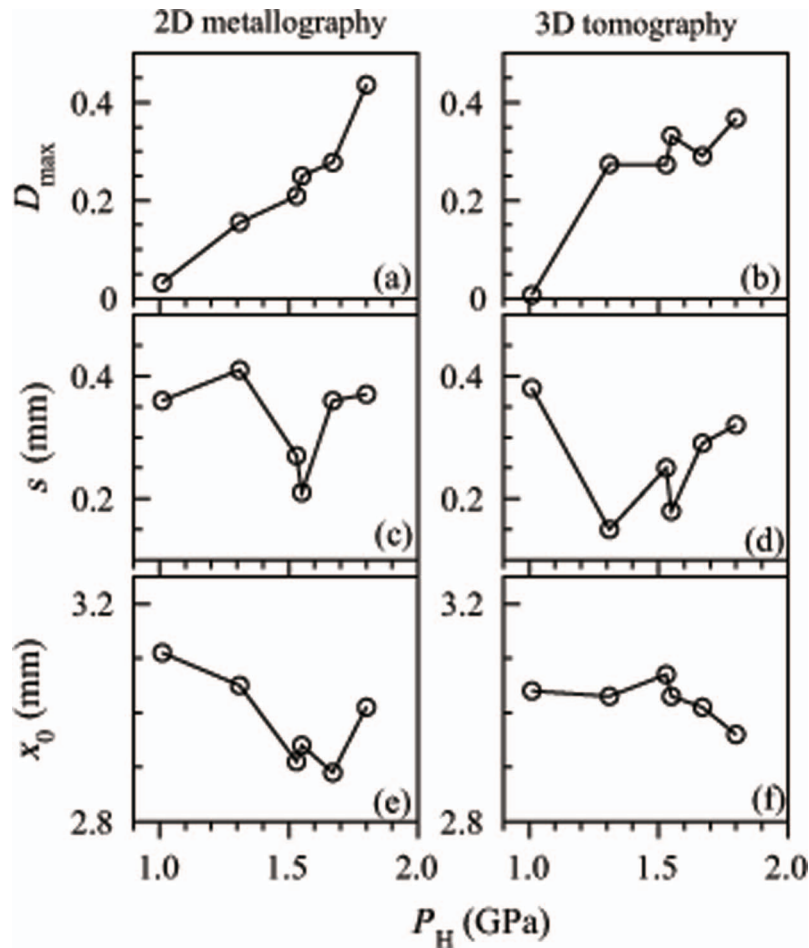


FIG. 5. Damage profile parameters [Eq. (7)] as a function of peak stress P_H , obtained from 2D metallography and 3D tomography.

measurements, on the other hand, represents the “true” damage measurements. We thus compare these two methods and quantify the relative errors in D_{\max} , σ , and x_0 measurements with 2D metallography, with respect to the true values obtained with 3D tomography (Fig. 6). The relative error of a quantity Q is defined as $|Q_{2D} - Q_{3D}|/Q_{3D}$. For D_{\max} , the 2D values appear to lie close to or below the 3D values, and the average relative error is 23%, excluding the outlier at the lowest impact velocity (149.6 m/s). There are four 2D data points are smaller than the 3D results. Part of the reason could be the inherent under-estimation by the Shwartz-Saltykov method.¹⁴ For σ , the 2D values are equal to or slightly larger than their 3D counterparts except an outlier at 170.0 m/s; the average relative error is 14% without the outlier. For x_0 , the 2D values are in excellent agreement with the 3D values within 3%.

Despite its simplicity, the 2D metallography method is a reasonable first-order characterization technique for ductile damage, and can predict the 1D damage profiles within an uncertainty of 10–25%. However, caution should be exercised given the possibility of outliers in 2D measurements, and sufficient statistics are desirable for reducing the scatter. In addition, sample preparation for metallography is also important since optical measurements are more susceptible to surface morphology than x-ray tomography with penetration capabilities.

The 3D tomography measurements also allow us to characterize void size distributions. We developed a code for such image analysis, and the code was validated against known microstructures and a commercial software AvizoTM. Figure 7 shows such distributions within a 0.3 mm slab centered on the spall plane, for different shock strengths. The voxel size is $1.5 \times 1.5 \times 1.5 \mu\text{m}^3$. The number

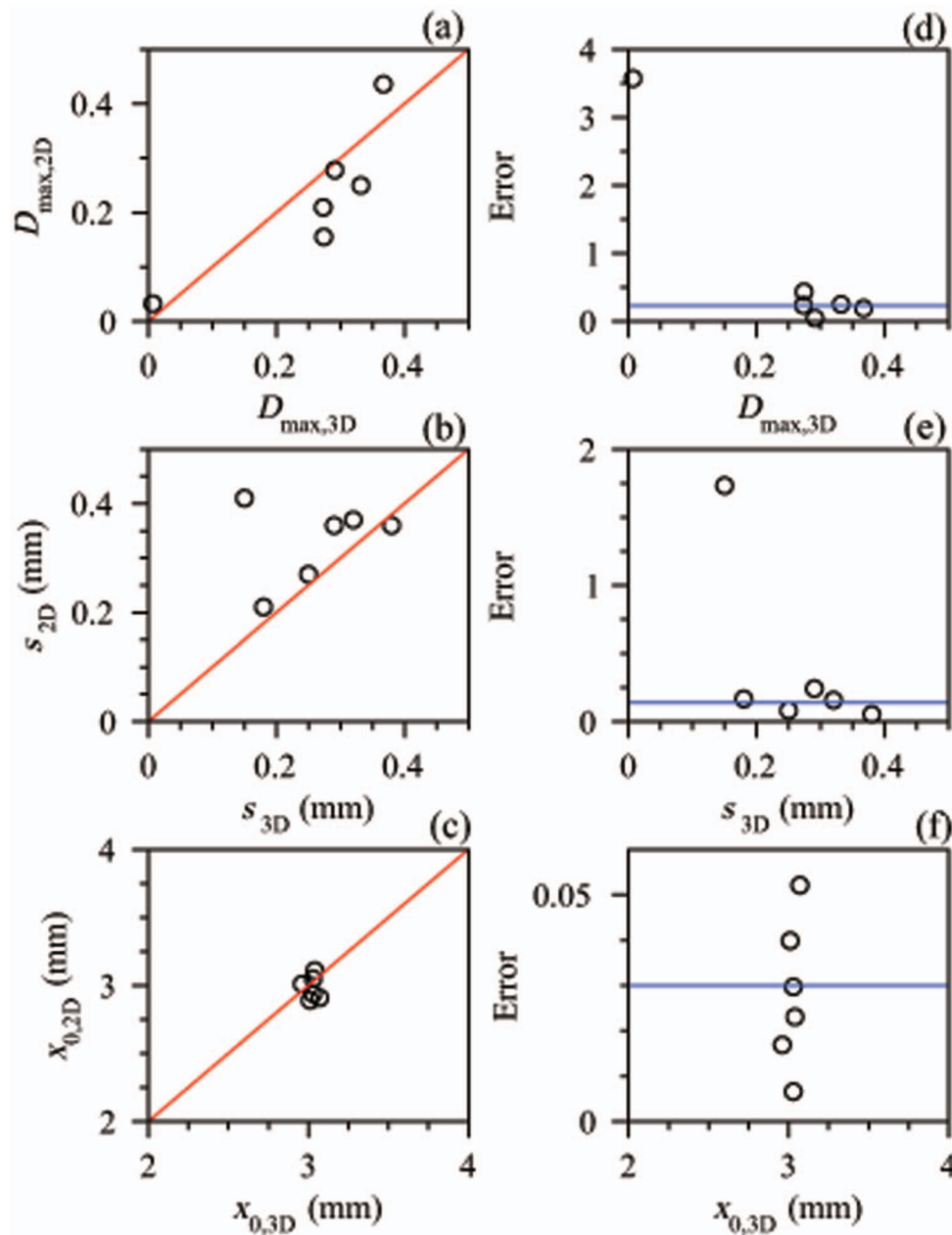


FIG. 6. Comparison of the values of D_{\max} (a), σ (b) and x_0 (c) measured with 2D metallography and 3D x-ray tomography, and corresponding relative errors (e–f). Also refer to Eq. (7). The lines in (a–c) denote $y = x$, and those in (e–f), the mean relative errors calculated without the outliers.

of voids (n_s) of a given size s , decreases with increasing size, and then $n_s(s)$ flattens, although the scatter in measurements does exist. The n_s -decreasing segment can be described with a power law

$$n_s = n_0 s^{-\gamma} \quad (8)$$

The fitting parameters n_0 and γ are plotted in Fig. 8 for different shock strengths (the exponents are also listed in Table I). The flat regime represents high connectivity of voids, i.e., void coalescence.

For 3D percolation models, the exponent γ is about 2.18, and similar values were found for the liquid droplet condensation near the critical point, and homogenous nucleation of melt.^{22–24} However, $\gamma \sim 1.4$ was reported for laser-spalled single-crystal Ta,¹⁸ in accord with our result. Zheng *et al.*²⁴

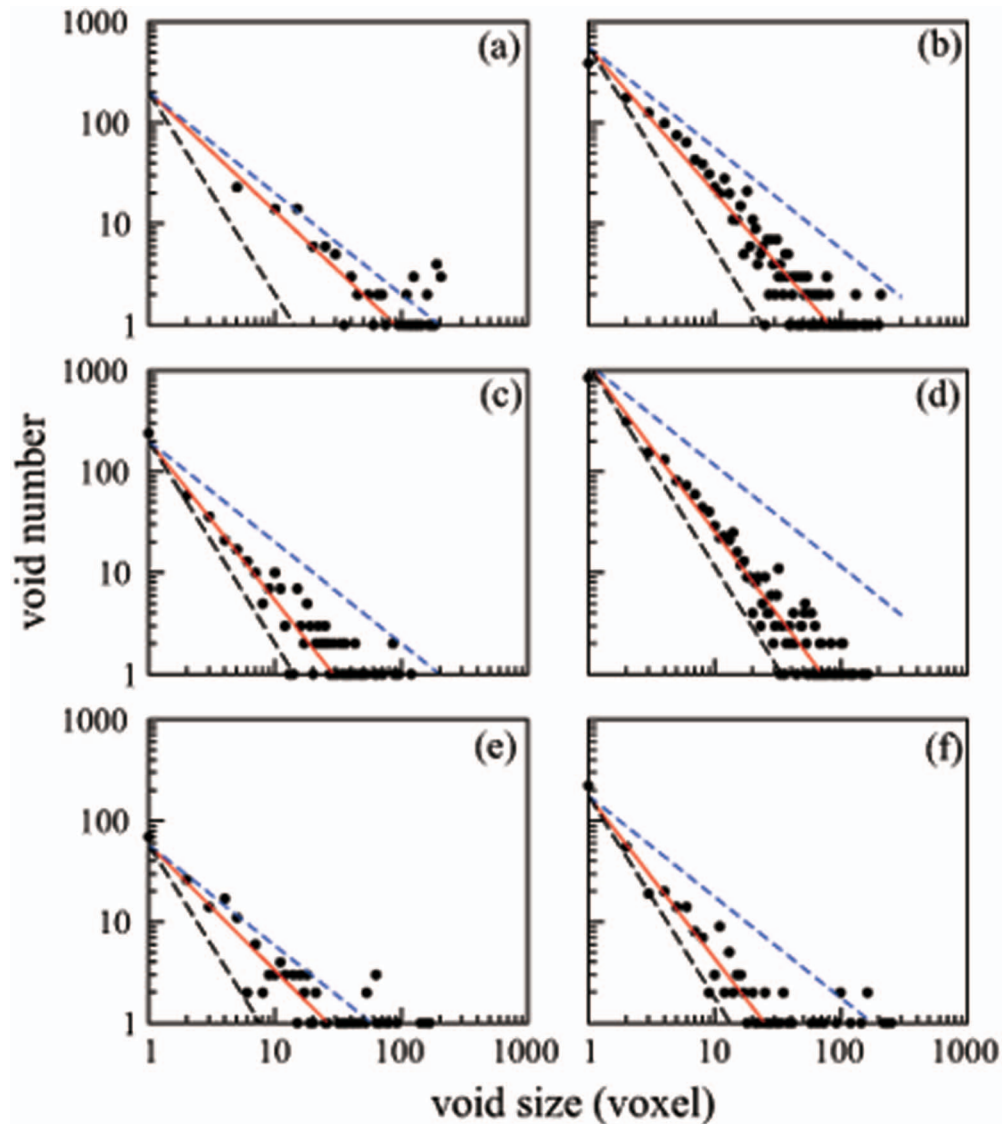


FIG. 7. Void size distributions near the spall plane (0.3 mm thick) for different impact velocities. (a)–(f) refer to $u_{\text{flyer}} = 149.6 \text{ m/s}$, 170.0, 196.9, 201.0, 215.4, and 236.3 m/s, respectively. The solid lines detones power law fittings $n_s = n_0 s^{-\gamma}$, and the dashed curves are plotted with $\gamma = 2$ (lower curve) and 1 (upper), respectively. Also see Table I.

suggested that the critical-sized nuclei form via percolation of subcritical nuclei during homogeneous melting, which could be analogous to formation of critical voids. However, γ is much smaller in our experiments, indicating a strong deviation from 3D percolation. Soulard *et al.*¹⁸ proposed three power laws for void nucleation, nucleation-growth, and nucleation growth-coalescence from their MD simulations, with decreasing exponents in that order. Other MD simulations observed decreasing exponent ($\gamma \sim 1-3.5$) at different times of spallation.²⁵ Damage in our experiments ranges from incipient to full spallation, with slightly increasing exponents (except for an “outlier” at $u_{\text{flyer}} = 215.4 \text{ m/s}$). The cause for the differences between simulations and experiments is unclear. The full spectrum of phenomenology and physical meaning behind the “power laws” remain to be explored. Spall damage depends both on loading (duration and shape) and microstructure,^{5,7,8,26} and thus systematic investigations of the dependence of damage on these factors are also desirable. Hopefully, a “scaling” law and scale invariance in spall damage can be obtained considering different materials, microstructures and loadings.

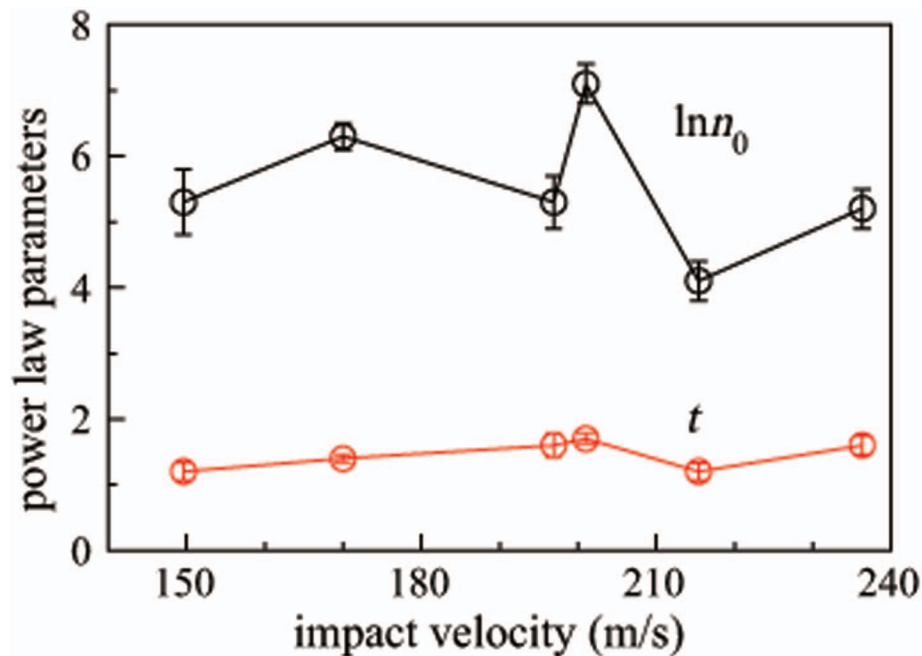


FIG. 8. Sensitivity of the power law fitting parameters to impact velocities. If treated as a constant, $\ln n_0 = 5.6 \pm 1.0$, and $\gamma = 1.5 \pm 0.2$.

IV. SUMMARY

We have characterized the spall damage in ultrapure Al induced by shock loading at different shock strengths with 2D optical metallography via the Schwartz-Saltykov method and 3D synchrotron x-ray tomography. The profiles can be well described with a Gaussian function and show appreciable dependence on shock strengths. The results from the 2D method are in accord with those from 3D tomography within 10-25%. Full tomography analysis shows that void size distributions follow a power law with an exponent of $\gamma = 1.5 \pm 0.2$, considerably smaller than the predictions from percolation models.

ACKNOWLEDGMENTS

We benefited from invaluable discussions with L. Q. Zheng, Q. An, L. Han, K. Xia and S. Huang. This work was funded by the National Natural Science Foundation of China and NSAF (11172221 and U1330111) and China Scholarship Council.

¹D. R. Curran, L. Seaman, and D. A. Shockley, "Dynamic failure of solids," *Phys. Rep.* **147**, 253–388 (1987).

²D. E. Grady, "The spall strength of condensed matter," *J. Mech. Phys. Solids* **36**(3), 353–384 (1988).

³M. A. Meyers, *Dynamic Behavior of Materials* (Wiley, New York, 1994).

⁴T. Antoun, L. Seaman, D. R. Curran, G. I. Kanel, S. V. Razorenov, and A. V. Utkin, *Spall Fracture* (Springer, New York, 2003).

⁵G. I. Kanel, "Spall fracture: methodological aspects, mechanisms and governing factors," *Int. J. Fract.* **165**:163(1–2), 173–191 (2010).

⁶A. J. Schwartz, J. U. Cazamias, P. S. Fiske, and R. W. Minich, in *Shock Compression of Condensed Matter-2001* (American Institute of Physics, 2001), Vol. CP620, p. 491.

⁷P. Peralta, S. DiGiacomo, S. Hashemian, S. N. Luo, D. Paisley, R. Dickerson, E. Loomis, D. Byler, and K. J. McClellan, "Characterization of Incipient Spall Damage in Shocked Copper Multicrystals," *Int. J. Damage. Mech.* **18**, 393–413 (2009).

⁸L. Wayne, K. Krishnan, S. DiGiacomo, N. Kovvali, P. Peralta, S. N. Luo, S. Greeneld, D. Byler, D. Paisley, K. J. McClellan, A. Koskelo, and R. Dickerson, "Statistics of weak grain boundaries for spall damage in polycrystalline copper," *Scripta mater* **63**, 1065–1068 (2010).

⁹J. P. Escobedo, D. Dennis-Koller, E. K. Cerreta, B. M. Patterson, C. A. Bronkhorst, B. L. Hansen, D. Tonks, and R. A. Lebensohn, "Effects of grain size and boundary structure on the dynamic tensile response of copper," *J. Appl. Phys.* **110**, 033513 (2011).

- ¹⁰D. Fan and M. L. Qi, "Microstructural evolution in void coalescence induced by plate-impact loading in ultrapure aluminum," *Adv. Mater Res.* **160–162**, 434–439 (2011).
- ¹¹H. A. Schwartz, "The Metallographic Determination of the Size Distribution of Temper Carbon Nodules," *Met. Alloys* **6**, 139–140 (1934).
- ¹²S. A. Saltykov, *Stereometric Metallography*, 2nd ed. (Metallurgizdat, Moscow, 1958).
- ¹³L. Seaman, D. R. Curran, and R. C. Crewdson, "Transformation of Observed Crack Traces on a Section to True Crack Density for Fracture Calculations," *J. Appl. Phys.* **49**, 5221 (1978).
- ¹⁴J. Takahashi and H. Suito, "Evaluation of the accuracy of the three-dimensional size distribution estimated from the schwartz-saltykov method," *Metal. Mater. Trans. A* **34**(1), 171–181 (2003).
- ¹⁵J. E. Hilliard and L. R. Lawson, *Stereology and Stochastic Geometry* (Springer, 2003).
- ¹⁶J. Bontaz-Carion and Y. P. Pellegrini, "X-ray microtomography analysis of dynamic damage in tantalum," *Adv. Eng. Mater.* **8**, 480–486 (2006).
- ¹⁷L. Jiang, N. Chawla, M. Pacheco, and V. Noveski, "Three Dimensional (3D) Microstructural Characterization and Quantification of Reflow Porosity in Sn-rich Alloy Solder Joints by X-ray Tomography," *Mater. Charact.* **62**, 970–975 (2011).
- ¹⁸L. Soulard, J. Bontaz-Carion, and J. P. Cuq-Lelandais, "Experimental and numerical study of the tantalum single crystal spallation," *Eur. Phys. J. B* **85**, 332 (2012).
- ¹⁹M. L. Qi, C. Luo, H. L. He, Y. G. Wang, D. Fan, and S. L. Yan, "Damage property of the incompletely spalled aluminum under shock wave loading," *J. Appl. Phys.* **111**, 043506 (2012).
- ²⁰M. D. Abramo, P. J. Magalhaes, and S. J. Ram, "Image Processing with Image," *J. Biophoton. Int.* **11**(7), 36–42 (2004).
- ²¹S. N. Luo, T. C. Germann, and D. L. Tonks, "Spall damage of copper under supported and decaying shock loading," *J. Appl. Phys.* **106**, 123518 (2009).
- ²²D. Stauer, *Introduction to Percolation Theory* (Taylor & Francis, 1992).
- ²³M. E. Fisher, "The theory of equilibrium critical phenomena," *Rep. Prog. Phys.* **30**, 615–730 (1967).
- ²⁴L. Q. Zheng, Q. An, Y. Xie, Z. H. Sun, and S. N. Luo, "Homogeneous nucleation and growth of melt in copper," *J. Chem. Phys.* **127**, 164503 (2007).
- ²⁵E. Leveugle, D. S. Ivanov, and L. V. Zhigilei, "Photomechanical spallation of molecular and metal targets: molecular dynamics study," *Appl. Phys. A* **79**, 1643–1655 (2004).
- ²⁶X. Chen, J. R. Asay, S. K. Dwivedi, and D. P. Field, "Spall behavior of aluminum with varying microstructures," *J. Appl. Phys.* **99**, 023528 (2006).